Vacuum 210 (2023) 111853

Contents lists available at ScienceDirect

Vacuum

journal homepage: www.elsevier.com/locate/vacuum

Improved performance of the NaFePO4/Hardcarbon sodium-ion full cell

S. Altundag [a], S. Altin [a], S. Yaşar [b], E. Altin [c,*]

[a] Inonu University, Physics department, 44280, Battalgazi, Malatya, Turkey
[b] Inonu University, Chemistry department, 44280, Battalgazi, Malatya, Turkey
[c] Inonu University, Vocational School of Health Service, 44280, Battalgazi, Malatya, Turkey

ARTICLE INFO

Handling Editor: Prof. L.G. Hultman

Keywords:
Na-ion
Ion exchange
$NaFePO_4$
Na-ion full cell

ABSTRACT

Chronoamperometry and galvanostatic procedures were applied in the $LiFePO_4$-based ion exchange approach for the production of $NaFePO_4$ cathodes. The materials obtained by various processes were employed as the cathode electrode in Na-ion half cells, and their structural and electrochemical properties were investigated. According to XRD patterns for both processes, it is seen that the Na-ions were successfully replaced with Li-ions. In addition of this, XPS and EDX-dot mapping analyses were supports the ion exchange procedure. The electrochemical properties of the cathode were investigated using CR2032 cells, and the diffusion coefficient and diffusion activation energy were calculated using the CV graphs at various scan rates and environmental temperatures. It was found that the Na-diffusion rate in the cell is faster at higher temperatures than at lower temperatures. The galvanostatic cycling tests were performed for C/10 and 1C rates at room temperature, 10 °C, and 50 °C and determined that the first capacities for C/10 and 1C at room temperature were 140mAh/g and 60mAh/g, respectively, with good stability. The full cells of $NaFePO_4$/hard carbon were fabricated by pre-sodiation technique and the battery performance tests revealed that the cells have a 74 mAh/g for C/10-rate with a voltage window of 2–4 V.

1. Introduction

After the discovery of Li-based rechargeable batteries, many lithium metal oxide electrode materials were found and used by commercial batteries. Among the cathodes, probably the most popular one is the battery cells made by $LiFePO_4$ since it is cheap, abundance of the components on the planet, and has high stability with a voltage plateau [1]. The need for battery storage has risen as people consume more energy than ever before, leading to the development of alternative battery chemistry that doesn't rely on lithium. Because of this, scientists have applied their understanding of lithium chemistry to the development of novel battery designs based on sodium, potassium, and other elements. Since sodium is in the same periodic table group as lithium, it has recently surpassed lithium as the element of choice as an alternative to lithium shares many of the same properties, is abundant on Earth, and has a low environmental impact. Furthermore, the most popular element instead of Li has seen sodium since it is in the same column as lithium in the periodic table and has similar properties, and is abundant on the planet with an environmentally friendly structure [2].

The most popular cathodes for Na-ion cells were seen as Na-metal oxide using Mn, Fe, Co, and Ni [3]. Among Na-ion cathode materials, olivine-type $NaFePO_4$ shows a high theoretical capacity (154 mAh/g) [4]. Although the analogy of $LiFePO_4$ with $NaFePO_4$ takes attention for the battery studies, the production of $NaFePO_4$ doesn't seem easy when compared with $LiFePO_4$ [5]. The most common techniques for the production of $NaFePO_4$ are seen in the ion exchange of $LiFePO_4$ and sedation of the $FePO_4$ phase [6]. Since $NaFePO_4$ is an important component of Na-ion batteries, researchers have developed different methods to synthesize it. C. Heubner et al. synthesized $NaFePO_4$ by the ion exchange method by three-electrode cells in 1 M $NaClO_4$ and tetraethylene glycol dimethyl ether [7]. They observed two charging peaks at CV as a result of sodium extraction, and the capacity was determined to be 125 mAh/g at a C/5 rate [8]. Then, Wongittharom et al. described the $NaFePO_4$ phase by electrochemical sodiation of the $FePO_4$ phase using an ionic liquid electrolyte. The cell formed with NaFePO4 synthesized by this method exhibit the capacity of 60 mAh/g and 120 mAh/g for 1C-rate and C/20-rate, respectively [9]. Consequently, it was determined that the highest performance by ion exchange was achieved at approximately 125 mAh/g [10–12]. Na-extraction energy of NaFePO4 was studied by Zheng et al. for various symmetries, providing

* Corresponding author.
E-mail address: emine.altin@inonu.edu.tr (E. Altin).

https://doi.org/10.1016/j.vacuum.2023.111853
Received 21 November 2022; Received in revised form 14 January 2023; Accepted 16 January 2023
Available online 18 January 2023
0042-207X/© 2023 Elsevier Ltd. All rights reserved.

insight into its production [13]. In addition, Lu et al. highlight the shift in crystalline structure as a function of Na-content when they examine the phase diagram of $NaFePO_4$ for varied Na content via ion exchange, solid-state synthesis, and chemical oxidation process [14]. As a result of these studies, the ion exchange process using galvanostatic methods is clearly the best method for producing $NaFePO_4$ [9,12].

Herein, we preferred to extract Li ions from $LiFePO_4$ employing galvanostatic charge and chronoamperometry and inserted the Na ions using the same methods. It was seen that the galvanostatic and chronoamperometry techniques used for the synthesis of $NaFePO_4$ from $LiFePO_4$ were successfully achieved and the chronoamperometry has an advantage for the shorter time to obtain $NaFePO_4$ phase when compared to the conventional galvanostatic technique.

2. Experimental section

Carbon-coated $LiFePO_4$ was employed as the basis material, and the specifics of its manufacture and cell assembly are described in Refs. [15, 16]. The $LiFePO_4$ cathodes were prepared by using $LiFePO_4$ powder/PVDF/carbon black in the ratio of 80/10/10 and they were mixed in NMP by MRX TM-300 vacuum mixer at −80kPa for 24 h and they were coated on the Al foil by a doctor blade. The obtained cathodes were stored in vacuum conditions for 2 days before the assembling of the battery cells in the glove box since the residual oxygen and H_2O may cause worse electrochemical properties than stored in a vacuum as seen in Ref. [17]. The CR2032 half-cell configuration was used for the ion exchange process under inert conditions. To extract Li-ions from $LiFePO_4$, we used the chronoamperometry technique and 4.3 V was applied up to current values below 1 μA. The galvanostatic charging process using C/20-rate before constant voltage charging (below 1 μA current value) was applied to extract more Li-ions in the cell. In the first production step, we also used different times to find out the optimum battery performance and it is found that 6 h charge is the best value for the delithation. A similar treatment was used for the sodiation process of the cell using 1.5 V values such as 2 h, 4 h, and 6 h (named LiNa6-2, LiNa6-4, and LiNa6-6, respectively) for the chronoamperometry and C/20 rate for the galvanostatic (named G-LFP) discharge process.

$LiFP_6$ in EC/DMC and $NaClO_4$ in PC/EC were used as the electrolytes for the ion exchange process and the experiments were performed in an argon-filled glovebox (Inert I-lab) with low oxygen and humidity values (<1 ppm). The calculation of gravimetric energy density of Na-ion cells was performed by accepting of all Li was exchanged by Na and the active mass of the cathode disc was assumed to increase by the ion exchange process due to differences in the molar mass of the $LiFePO_4$ (157.757 g) and $NaFePO_4$ (173.806 g). For example, the active mass of the electrode was calculated as 3.25 mg for LiFePO4 and when the ion exchange procedure was performed, we used the mass of 3.58 mg for the $NaFePO_4$ cell for the same electrode. The full cells were made using hard carbon as an anode and presodiation process of the anode was made by galvanostatic charge/discharge for C/10-rate.

Fig. 1a and b show the results of chronoamperometry and galvanostatic charge/discharge process for the production of $NaFePO_4$ from $LiFePO_4$ cathodes, respectively. Fig. 1 c illustrates the expected ion exchange mechanism for the production of the $NaFePO_4$ cathodes. The used experimental conditions are given in Table 1.

The XRD patterns of the ion-exchange cathodes were measured by Rigaku RadB Dmax. The FTIR analyses of the samples were performed by PerkinElmer (Spectrum One) and the surface photographs and EDX analysis of the samples were obtained by Leo EVO-40 VPX with a combined Bruker EDX detector. The XPS analysis of the cathode was measured by the Thermo Scientific K-Alpha system with a monochromatic Al-Kα source at EMUM-Izmir-Turkey. It should be noted that Aligning the spectra to the C_{1s} peak of adventitious carbon is not reliable as it may lead to unphysical results. Adventitious carbon is in general an unknown compound, not an inherent part of the sample, and does not make proper electrical contact with the analyzed sample [18–23]. The

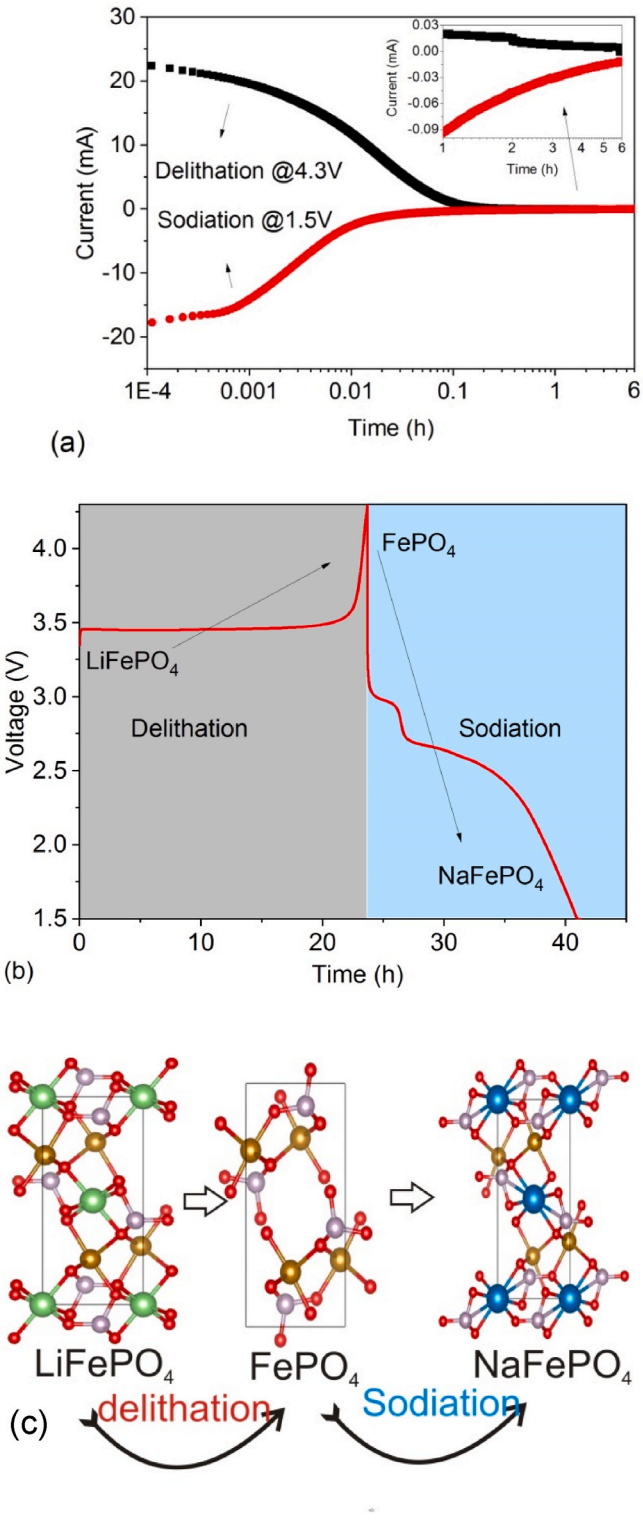

Fig. 1. (a) Cronoamperometry measurement for Li-extraction and Na-insertion for 6 h charge and discharge, (b) galvanostatic technique for C/20 and ion exchange and (c) schematic illustration of the mechanism of the ion exchange of Na by Li in the lattice.

emission source of monochromatic radiation was an Al- K_α source of 1486.68 eV, at a voltage of 12 kV and a current of 6 mA. The electron gun for charge compensation was activated. The measurement spot size was ~400 μm and the beam current was 4.2 mA. The calibration of the XPS system was performed by gold foil and the Au-4f7/2 core level of

Table 1
Experimental conditions for the production of $NaFePO_4$ cathodes.

Charging	Discharging @1.5 V
6 h@4.3 V (Const. Volt.)	2 h@1.5 V (Const. Volt.) 4 h@1.5 V (Const. Volt.) 6 h@1.5 V (Const. Volt.)
C/20 for ≤4.3 V (Const. current.)	C/20 for ≥1.5 V (Const. current.)

gold was set to a binding energy of 84.0 eV [24] and the detailed procedure of the XPS analysis can be found in Ref. [25]. Before the calibration, the Au foil surface was cleaned by Ar + ion-etching due to the possibility of surface contamination. The pressure of the system was kept at below 5×10^{-10} mbar for the period of data acquisition. The XPS survey scans (−10 - 1350 eV) were done for the electrode with the pass energy at 150 eV and step size at 1 eV. Narrow scans of each element were done at pass energy of 50 eV and step size of 0.1 eV. It is well known that correct measurement of binding energy by XPS analysis is important for reliable data. The calibration of XPS data can be performed by using the equation of the C 1s peak at $E_B = 289.58 - \varphi_{SA}$ eV where E_B is the binding energy and φ_{SA} is the work function and the formula is not expected to work properly for poorly conducting samples that are prone to charging [26]. Although the φ_{SA} can be measured by ultraviolet photoelectron spectroscopy attached to the XPS system, it also can be used from the existing studies as 4.81 eV for carbon [27] and binding energy of C1s calculated as 284.77 eV which was used for the calibration of the XPS data in this study [28]. TEM-EDX measurements were performed by JEOL JEM-1400 Plus combined with Oxford Instruments X-Max EDX detector (at Cobiltum research center, Canakkale-Tukey). To prepare the sample for TEM-EDS analysis, the ion-exchanged cathode was dissolved in NMP by magnetic stirrer overnight and ultrasonically mixed for homogenization and dropped 10 mL on a copper grid, and then dried at 120 °C for several hours. The detail of the assembling of the battery cells and performance tests can be found in our previous paper [15,16].

3. Results and discussion

3.1. Structural analysis

To fabricate $NaFePO_4$, first, we fabricated and characterized $LiFePO_4$ powders by XRD analysis. The XRD patterns of synthesized $LiFePO_4$ powder and electrodes on Al foil were presented in Fig. 2a. X-ray diffraction analysis showed that the powders have no impurity phases and a good fit with the $LiFePO_4$ diffraction line [29]. In the cell, Li ions were extracted from the $LiFePO_4$ structure, and the resulting XRD patterns are shown in Fig. 2. The change of the diffraction line was clearly observed in the XRD pattern, and the diffraction lines of the $FePO_4$ phase were also presented in Fig. 2. After Na-insertion in $FePO_4$ lattice by various procedures, the structure of the samples was analyzed by XRD, as shown in Fig. 2a, and it was determined that the XRD pattern was consistent with $NaFePO_4$ diffraction lines [30]. However, some $LiFePO_4$ impurity phases were observed in the $NaFePO_4$. To identify the lattice parameters and phases formed during to ion exchange process, we calculated the lattice parameters by GSAS-II software (the fitting curves are presented in Fig. S1 and the results were presented in Table 2. The ratio of $FePO_4$ phases is seen to be 98.1% and 97.5% for chronoamperometry and galvanostatic charged samples with impurity phases of $LiFePO_4$ with ratios of 1.9% and 2.5%, respectively. The lattice volume was calculated as 278.657 $Å^3$ ($LiFePO_4$) and 269.990 $Å^3$ ($FePO_4$) for 6 h charged by chronoamperometry technique and as 297.837 $Å^3$ ($LiFePO_4$) and 279.195 $Å^3$ ($FePO_4$) for C/20 discharge.

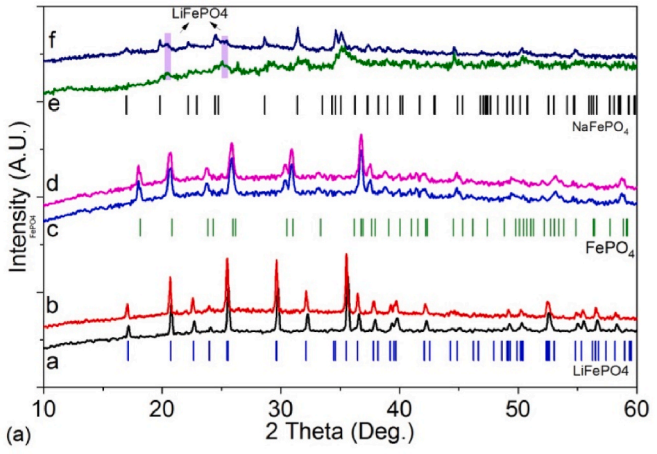

Fig. 2. XRD pattern of the samples (a: $LiFePO_4$ powders, b: $LiFePO_4$ electrode on Al, c: charged 6 h using chronoamperometry and d: C/20 charged (galvanostatic), e: discharged 6 h using chronoamperometry and f: C/20 discharged (galvanostatic)).

In our prior work, the lattice parameters of unprocessed LiFePO4 were reported as a = 10.320 Å, b = 6.007 Å, and c = 4.692 Å with a volume of 290.909 Å [15,16]. The computed lattice volumes of the residual $LiFePO_4$ for the chronoamperometry and C/20 discharge methods were calculated as 278.657 $Å^3$ and 299.813 $Å^3$, respectively, after the Li-de-insertion procedure.

To understand the differences in the lattice volume of the residual $LiFePO_4$ phase, we also take into account the main phase of $FePO_4$ and it is found that the lattice volume of $FePO_4$ was found as 269.99 $Å^3$ for chronoamperometry and 271.174 $Å^3$ for C/20 discharge. It is known that $LiFePO_4$, $FePO_4$, and $NaFePO_4$ possess the same Pnma lattice symmetry, and the decrease in lattice volume during the discharge process shows the de-lithiation of the lattice. The Sodiation procedure was carried out for both procedures, and the phase fraction and lattice parameters are presented in Table 2.

Chronoamperometry and galvanostatic methods reveal that the main phase is 95.4% and 99.5% $NaFePO_4$ with impurities of 4.6% and 0.5% $LiFePO_4$, respectively. In addition, the lattice volume was calculated as 328.258 $Å^3$ and 318.194 $Å^3$ for chronoamperometry and galvanostatic techniques, respectively. Based on the change of lattice volumes of the samples during the de-lithiation and sodiation processes via both techniques, it can be predicted that the fast ionic movement in the lattice causes the deformation of the lattice. Therefore, the chronoamperometry technique caused a greater change in lattice volume.

FT-IR spectrums of the $LiFePO_4$ powder, $LiFePO_4$ electrode, and delithation and sodiation electrode with different process forms were given in Fig. S2. Different bands in the structure for the powders were attributed to the characteristic bands of Fe–O and P–O bonds at 581 cm^{-1} and at 469 (the doublet ν_2). The characteristic bands at 499, 551, and 637 cm^{-1} (all are due to triplet ν_4) are attributed to PO_4^3—bonds in $LiFePO_4$, and bands at 962 cm^{-1} (symmetric ν_1), 1077 cm^{-1}, and 1136 cm^{-1} (asymmetric ν_3) can be attributed to two P–O bonds [27]. The trigonal FePO4 exhibited a broad maximum between 900 and 1200 cm^{-1} which can be assigned to the P–O vibrations. It is stated that the bands at 430, 648, 592 cm^{-1} (Fe–O–Fe), and 891, 1027, 1097 cm^{-1} (Fe–O–P) serve as an identity of iron phosphate [31,32]. In addition, the Li–O bands were observed at 455.1 cm^{-1}, 508.9 cm^{-1}, 719.7 cm^{-1}, 810.4 cm^{-1}, 1093.9 cm^{-1} [33]. So it is predicted that the Li–O vibration bands overlap with P–O bands in the $LiFePO_4$.

When looking at the FTIR spectrum of sodiated electrode, the bands detected between 900 and 1150 cm^{-1} are attributable to symmetric ($\nu 1$) and asymmetric ($\nu 3$) stretching modes, whereas the bands between 500 and 650 cm^{-1} are associated with symmetric ($\nu 2$) and asymmetric ($\nu 4$) bending modes [34]. In particular, the distinctive stretching and bending vibrations of the phosphate anion $(PO4)^{3-}$ are well delineated in the FTIR spectrum. While the stretching modes are observed at 974.5 cm^{-1} ($\nu 1$) and 1023 cm^{-1} ($\nu 3$), the bending modes are observed at 566.3 cm^{-1} ($\nu 4$) and 627.6 cm^{-1} ($\nu 2$) for the phosphate anion $(PO4)^{3-}$

Table 2
Lattice parameters and phase fraction in the cells.

Sample	phase	a (Å)	b (Å)	c (Å)	V (Å^3)	Phase Fraction %	w_R
6 h Ch.	LiFePO4	10.207 (9)	6.042(5)	4.518 (4)	278.657(3)	1.9	2.96%
	FePO4	9.801 (2)	5.776 (1)	4.769 (1)	269.990 (1)	98.1	
6 h DisC.	LiFePO4	9.915 (10)	6.240 (8)	4.846(6)	299.813 (1)	4.6	3.40
	NaFePO4	10.519 (6)	6.256 (4)	4.988 (3)	328.258 (2)	95.4	
Galv. C/20 Ch.	LiFePO4	11.146 (3)	5.890 (1)	4.537 (1)	297.837 (2)	2.5	3.02%
	FePO4	9.810 (1)	5.785 (2)	4.778 (1)	271.174 (2)	97.5	
Galv. C/20 DisC.	LiFePO4	9.617 (5)	5.994 (3)	4.844 (3)	279.195 (3)	0.5	3.24%,
	NaFePO4	10.400 (3)	6.205 (2)	4.931 (2)	318.194 (2)	99.5	

[35,36]. The addition of PVDF, NMP, and carbon during to electrode preparation process led to the observation of the weak bands at 1182 and 1590 cm^{-1} which are ascribed to the stretching vibrations of the C–O bond. and band at 2304 cm^{-1} is assigned to C–H stretching vibrations [37,38]. It is reported that Na_2O has bands at 890 cm^{-1} and 1430 cm^{-1}, and these frequencies matched the findings of the present results [39,40].

Figs. S3a–c illustrates the elemental dot mapping outcomes of the bare $LiFePO_4$ electrode, 6 h discharged and 6 h charged using chronoamperometry. As expected, there is no indication of the presence of Na ions, however, Fig. S3 c reveals the existence of Na ions in the structure that are uniformly distributed across the surface of the electrode. The elemental ratio of the bare electrode was measured to be 43.93/56.07 for Fe/P, whereas the ratios for the delithated and sodiated electrodes were 45.72/54.28 for Fe/P and 26.7/35.26/38.02 for Na/Fe/P, respectively. Therefore, the expected chemical formula of the sodium cathodes was estimated as $Na_{0.75}FeP_{1.07}O_4$ and the Fe/P ratio should be near 1, and it is noticed that a portion of Na is not incorporated into the structure; the impact of this inefficiency was observed in the analysis of battery performance, as mentioned in the following sections.

Fig. S4 shows the TEM analysis results of cathodes for 6 h charged and 6 h charge/6 h discharged and it is seen that the particle size was observed as ~50 nm. The EDX results of the particles in TEM images were presented in Fig. S4 and it is found that the Na-ions were inserted into the grains. Although the Na content was less than the expected value, we can say that the ion exchange process was achieved in the

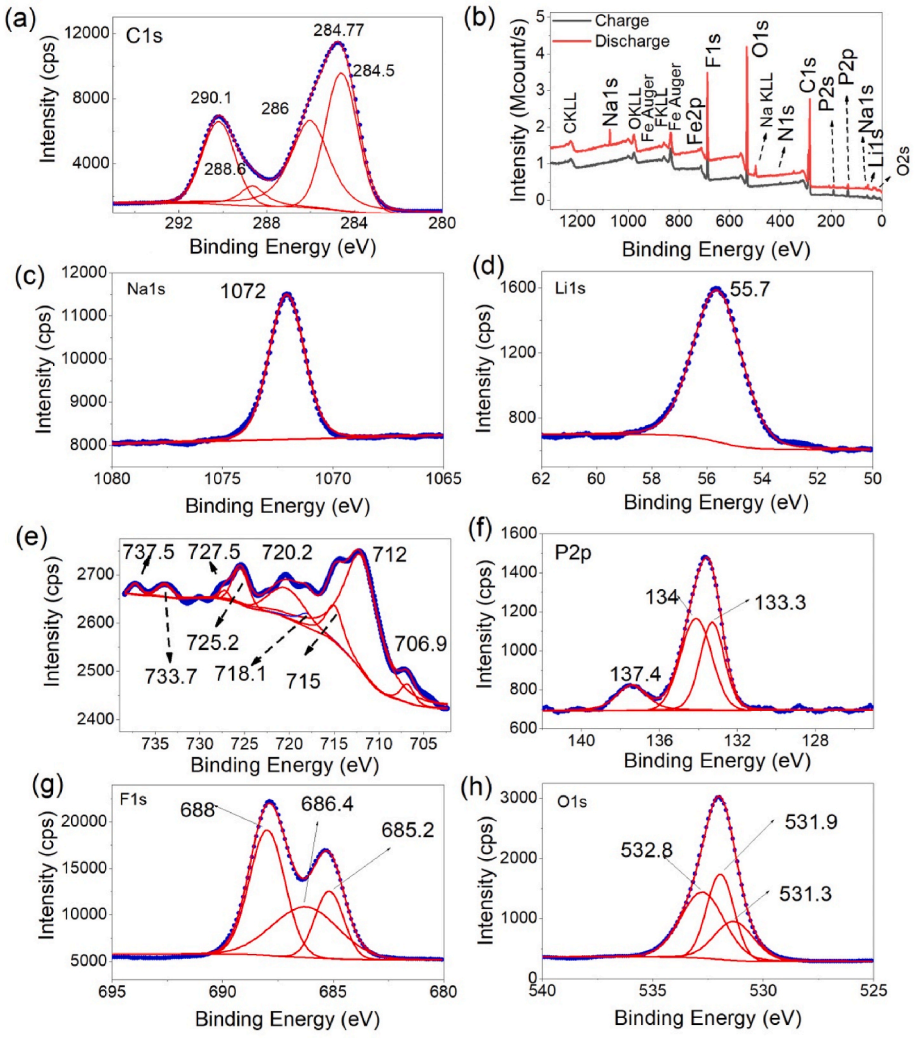

Fig. 3. (a) Carbon and (b) survey, (c) Na1s, (d) Li1s, (e) Fe2p, (f) P2p, (g) F1s and (h) O1s XPS spectra for 6 h charged and 6 h charge/6 h discharged.

cells. It should be noted that the Na content in the structure will increase during the cycling cells of the battery cells.

Fig. 3 a shows C1s XPS spectra and the C–C/C–H peak was observed at 285.1 eV which has a difference of 0.33eV and all spectrum was calibrated using this value. Fig. 3 b illustrate the XPS survey spectra of both charged and discharged electrodes and it was observed the electrolyte-related peaks visible in the $LiPF_6$, $NaClO_4$, and additives such as EC, DMC, PC at the spectrum. The primary objective of the XPS analysis is to demonstrate the existence of Na-ions following the discharging operations depicted in the image. Despite the fact that the surface of the electrodes was cleaned with EC before XPS tests, we observed that a portion of the electrolyte contents in the analysis was due to $LiPF_6$, $NaClO_4$, and electrolyte additives (PC, EC, and DMC). The elemental ratios of the XPS measurements were presented in Table S1 and the results are consistent with TEM-EDX results of the samples.

It was observed two main peaks (284.77 eV and 290.1 eV after calibration) in XPS spectra of C1s as seen in Fig. 3 a with four different sub-peaks at 284.5 eV (C═C), 286 eV (C–O), 288.6 eV (C═O) [41], and 290.1 eV (OH–C═O) [42] and it should be related to electrolytes and additives in the cells. Fig. 3c and d show the XPS spectra of Na1s and Li1s and it is observed that there is one peak at 1072 eV and 55.7eV which corresponds to Na1s and Li1s in the cathode, respectively. In the energy region of Na1s, the XPS spectra of the pristine electrode are composed of the signal having binding energies corresponding to Na^+ in the NaF compound. The origin of NaF is the result of the electrode fabrication where PVDF is used as a binding substance. The existence of surface NaF is also approved by the F1s spectrum: there are two overlapping signals of binding energies 688 and 685.2 eV that are related to F^- ions in PVDF and NaF, respectively. According to the previous XPS studies on electrode surfaces [43], the signal at 686.4 eV can be attributed to F^- ions in decomposed products of the lithium salt such as $Li/Na_xPF_yO_z$ (Fig. 3g). In the XPS spectra of Li1s, an intensive signal (55.7 eV) coming from Li^+ ions in LiF appears after the electrochemical reaction. During the ion exchange process, the binding energies of Li and Na have special importance since the applied voltage values for the both delithation and sodiation process are related to the binding energy of the ions. Although we measured the Na1s core level with the binding energy of 1072 eV, the Na2s measurement can be compared with Li1s binding energy for the prediction of the ion exchange process. It is stated that the Na2s binding energy (~63.8 eV) is higher than that of Li1s (55.7 eV) and the ionic radii of the cations decrease in the order $Na^+ > Li^+$ which is important for the ion movement in the lattice structure [44]. So it is predicted that the delithation process from the lattice is easier than that of presodiation due to the difference in the binding energy and ionic radii of the ions. Fig. 3 e presents the XPS spectra of Fe2p and it was observed 9 different sub-peaks at 706.9 eV (Metallic Fe), 712 eV ($Fe^{2+}2p_{3/2}$), 715 eV ($Fe^{3+}2p_{3/2}$), 718.1 eV (satellite of $Fe^{2+}2p_{3/2}$), 720.2 eV(satellite of $Fe^{3+}2p_{1/2}$), 725.2 eV ($Fe^{2+}2p_{1/2}$), 727.5 eV ($Fe^{3+}2p_{1/2}$), 733.7 eV (satellite of $Fe^{2+}2p_{1/2}$) and 737. 5 eV (satellite of $Fe^{3+}2p_{1/2}$) [45–48]. It should be noted that the metallic Fe peaks may come from the Al foil (MTI corp. Purity > 99.3%) as a current collector in the cell and there are Fe^{2+} and Fe^{3+} peaks on the surface of the cathode. The expected result of the Fe valence state on the $NaFePO_4$ is 2+ and the 3+ valence state of Fe should be due to the contact of an electrode in the air during the opening of the sealed cells. Fig. 3f shows the XPS spectra of P2p with three different peaks at 133.3 eV ($P2p_{3/2}$), 134 eV ($P2p_{1/2}$), and 137.4 eV (P_xO_y) [49]. It was observed three different oxygen sub-peaks in Fig. 3h at 531.3 eV (Metal-OH), 531.9 eV (CO_3^{2-}), and 532.8 eV (Metal-O) [49] for O1s.

3.2. Electrochemical analysis

3.2.1. Half cells tests

Fig. 4 a depicts the CV graphs of the $LiFePO_4$/Li and $NaFePO_4$/Na cells obtained by the chronoamperometry method for various discharging times and galvanostatic procedures. It was discovered that the

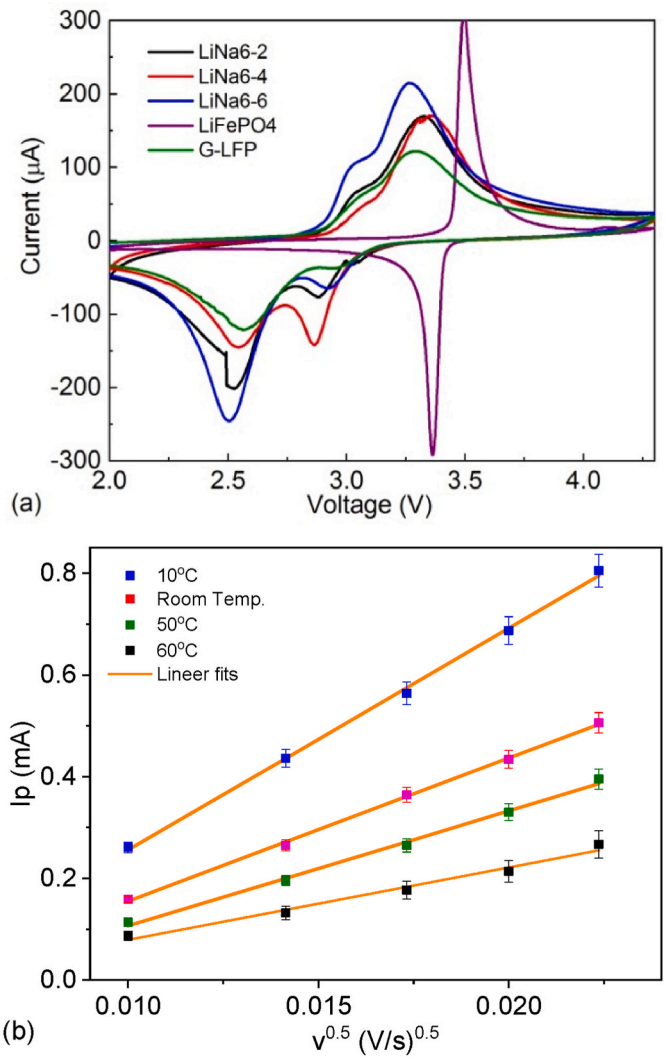

Fig. 4. (a) CV graphs of the LiNa6-2, LiNa6-4 and LiNa6-6 samples and (b) 1000/T-lnD curve of the cell produced chronoamperometry method for LiNa6-6.

redox peaks of $LiFePO_4$ are 3.50V/3.37 V, which is the expected value for $LiFePO_4$ half cells [50,51]. It is common knowledge that there are one Li-site and three separate O-sites that are the nearest ions to Li in the lattice. The Li–O bonds are found as 2.033 nm, 2.148 nm, and 2.163 nm in the structure. During the charge/discharge process, one redox reaction is detected and it is predicted that the crystal field around Li ions is nearly the same and that the barrier energy for the delithation process creates one energy level without splitting it. However, the lengths of Na–O bonds were calculated as 2.308 nm 2.310 nm and 2.415 nm for the $NaFePO_4$. Due to electrostatic interactions in the lattice, the crystal field surrounding Na ions is smaller than that surrounding Li ions, thus the barrier energy for desodiation should be lower than in $LiFePO_4$. When the crystal field goes weaker value, the bond lengths cause the splitting of energy value for desodiation process. In addition, the barrier energy for Na-movement in the structure should be shared between two distinct pathways for the desodiation process in the structure. The weaker bond length causes the weaker crystal field and redox energy in the CV graphs. Therefore, we hypothesize that the 3.05V/2.51 V and 3.29V/2.87 V redox reactions are caused by changes in the bond lengths and crystal fields around the Na-ions in the structure. According to Fig. 4a, all samples exhibit a successful Li-to-Na exchange in the structure, and the CV graphs are comparable to those of existing NaFePO4/Na cells [52, 53]. We also measured the CV at different temperatures to see the

change in the redox mechanism for the cells and used the cell, which was prepared by chronoamperometry technique for 6 h charge and 6 h discharge. Figs. S5a–d shows the CV graphs of C 6-6 cells for different scan rates at 10 °C, room temperature, 50 °C and 60 °C. According to CV graphs, the CV peak current and the square root of the scan rate show a linear change as observed in Fig. 4 b, where the diffusion coefficient of the Na-ions can be calculated by using the Randles–Sevcik equation provided below [54]:

$$I_p = 0.4463 \bullet n^{\frac{3}{2}} F^{\frac{3}{2}} \bullet C \bullet A \bullet R^{-\frac{1}{2}} T^{-1/2} D^{1/2} v^{1/2}$$

where the I_p is the maximum peak current value in CV graphs, n is the electron number, F is named as the Faraday constant, C is the Na-ion concentration, and A is the surface area of electrodes which is obtained with the BET surface area presented in Table S2, R is the rayleigh constant, T is the temperature in Kelvin unit, D is the diffusion coefficient of the Na-ions, and v is the CV scan rate. I_p vs. $v^{0.5}$ graphs were presented in the slope of Fig. 4 b and it was observed a linear change in the graphs. The D (m^2/s) values obtained from Fig. 4 b were found as 2.468(±0.02) x 10^{-12}, 3.824(±0.03) x 10^{-12}, 9.154 (±0.03) x 10^{-12} and 11.526(±0.03) x 10^{-12} for 10 °C, rt, 50 °C and 60 °C, respectively. As anticipated, it is predicted that the D values will grow as the temperature rises. The Arrhenius equation can be used to compute the diffusion activation energy, which is essential for understanding the diffusion mechanism. The slope of 1000/T-lnD graphs gives the activation energy for the diffusion and is found as 1.05(±0.03) eV for this sample (Fig. S5e).

Figs. S6a–c depicts the Voltage-Capacity graphs of LiNa6-6, LiNa6-2, LiNa6-4, and G-LFP, respectively, for C/10-rate up to 100 cycles, and the highest initial capacities were obtained for the LiNa6-6 and G-LFP. The Capacity-cycle number graphs were displayed in Figs. S6d and a wide peak followed by a decrease was noted for all cells. The obtained specific capacity values from Fig. S6 d were presented in Table 3. Figs. S6e–g depict the Voltage-Capacity graphs of LiNa6-6, LiNa6-2, LiNa6-4, and G-LFP for 1C-rate. According to the graphs, the capacities of G-LFP and LiNa-66 are almost identical. Fig. S6h depicts the capacity-cycle number for 1C-rate, and a capacity jump region was detected in the LiNa6-2 and LiNa6-4 cells. After 50 and 33 cycles, the capacity values of these cells exhibit improved performance, respectively. However, this capacity jump region was not observed for LiNa6-6 and G-LFP cells. These jumps are attributed to residual Li-ions in the structures, which contribute to the cell's cycling process which supports TEM-EDS and XPS results.

Table 3
The galvanostatic test result of the half cells.

Sample	C- value	1.Cycle	20.Cycle	50.cycle	100.cycle	250.cycle
LiNa6-2	C/10	81.1	112.9	111.8	91.8	–
	C	40.6	40.5	36.8	50.9	63.2
LiNa6-4	C/10	92.9	122.5	113.5	93.6	–
	C	37.2	35.2	39.6	50.5	56.6
LiNa6-6	C/10	111.1	127.1	119.6	106.1	–
	C	52.5	55.4	53.7	55.3	58.8
G-LFP	C/10	112	116.4	110.6	79.7	–
	C	50.6	47.5	46.0	47.8	48.25

Capacity (mAh/g)	Capacity fade %	Explanation	Ref.
125 at 1C	35 for 100 cycles	0.5 M NATFSI incorporated IL electrolyte was used	[9]
120 at C/20	–	1 M NaClO4 in PC electrolyte	[14]
125 at C/5	0.1 per cycle up to 50	1 M NaClO4 in TEGDME	[7]
140 at C/10	92 for 200 cycles	1 M NaClO4 in PC/EC (1:1 in volume) with 5% FEC	[55]
125 mAh at C/20	–	1 M NaClO4 in 98% PC and 2%FEC electrolyte	[56]
111 mAh at C/10	10 for 240 cycles	1 M NaPF6 in EC/DEC	[57]

The theoretical capacity of $NaFePO_4$ is 154 mAh/g.

Table 3 presents the capacity values for various C-rates, and the LiNa6-6 cells exhibit the highest performance among the cells. The capacity of previous $NaFePO_4$ research was also provided in Table 3, and it can be seen that the chronoamperometry approach has the ability to produce this phase in less time than the others, as the acquired capacity is comparable to that of current studies.

Fig. 5a–c depicts the voltage-capacity graphs at 50 °C and 10 °C up to 100 cycles, as well as the capacity cycle number graphs. It is observed that the cell capacities are 161 mAh/g at 50 °C and 98 mAh/g at 10 °C, respectively. While the capacity fade values of the cells at 50 °C were obtained as 50% for 100 cycles, the negative capacity fade was observed for low temperatures. Consequently, it can be stated that the battery performance of the cells is stable at room temperature and below room temperature.

Fig. 6 depicts the C- rates for all samples evaluated in this study. The various rates were executed at the present rates of C/10, C/5, C/3, 1C, and 2C. It is evident from this figure that LiNa6-6 cells exhibited the highest rate of performance.

Fig. S7 presents the EIS analysis results of LiNa6-2, LiNa6-4, LiNa6-6, and G-LFP, and the equivalent circuit model was presented in the inset of Fig. S7. In the equivalent circuit, R_s and R are defining the solution resistance and the charge transfer resistance between the electrode and electrolyte interface, respectively. The semi-circle in EIS (R) is due to Na^+ migration in the high-frequency region, and C is explained by the pseudo-capacitance at the interface between the electrode and electrolyte [58]. The Warburg diffusion element (W) is a parameter related to bulk diffusion resistance and Q is the constant phase element (roughness of the electrode surface) in the cells [59,60]. The obtained fitting parameters are provided in Table 4, where it can be observed that the lowest Rs, R, W, and C values were found for the LiNa6-6 cell, which has the highest battery performance.

3.2.2. *Full cell tests by Cr2032 cells*

Fig. 7 a depicts the NaFePO4/hard carbon full-cell CV graphs for two cycles, with one anodic and one cathodic peak detected in the half-cell CV. Fig. 7 b depicts the EIS analysis of the NaFePO4/hard carbon cell, whereas the inset of Fig. 7 b depicts the model-fitted data.

The obtained parameters were presented in Table S3. It is seen that the model fitting of the half cells is different from the full cells which are expected results since the anode, cathode, and electrolyte interactions make contributions to the EIS measurements of full cells. Fig. 7 c depicts the C-rate data of full cells between 2 V and 4 V; it can be observed that the cells' capacity exceeds 80 mAh/g for C/10 and then declines to 9 mAh/g for 2C-rate.

Fig. 8a depicts the capacity voltage graphs for C/10-rate up to 100 cycles, and the capacity value is determined to be 74 mAh/g for 1. cycle before decreasing to 49 mAh/g. Fig. 8b illustrates the graphs of capacity voltage for C/2-rate up to 100 cycles. The initial capacity value is 43 mAh/g, followed by a decline to 16 mAh/g. The capacity fade values were calculated to be 0.33 and 0.63 based on the capacity cycle number graphs presented in Fig. 8c. According to the number of cycles, the coulombic efficiency values approach 100%.

4. Conclusion

In this study, LiNa6-2, LiNa6-4, LiNa6-6, and G-LFP cathodes were effectively synthesized utilizing an ion-exchange approach with $LiFePO_4$ electrodes, and their structural and electrochemical properties were examined. $NaFePO_4$ was discovered to be the main phase of cathodes following ion exchange using two distinct approaches. The estimated chemical formula of the sodium cathodes was found as $Na_{0.75}FeP_{1.07}O_4$ from SEM-EDX analysis and it is noticed that a portion of Na is not incorporated into the structure and the elemental ratio obtained from TEM-EDX and XPS are lower than that of SEM-EDS which explained the investigation of small and surface area of the samples. The CV of the cells showed that the ion exchange procedure was successfully achieved for

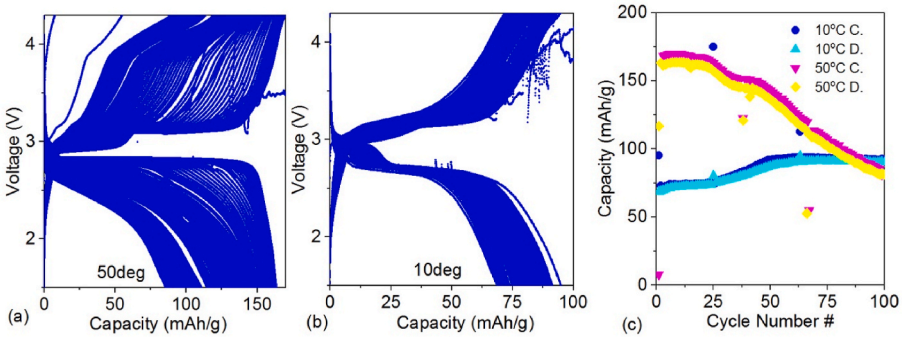

Fig. 5. Capacity-voltage graphs at (a)50 °C, (b) 10 °C and (c) Capacity-cycle number graphs of LiNa6-6.

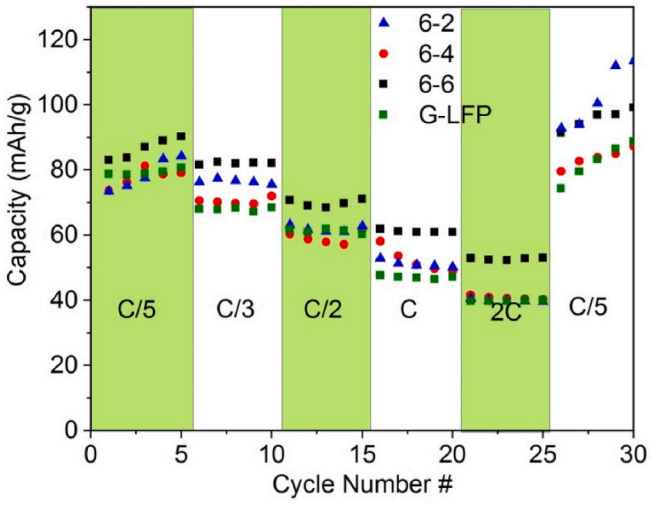

Fig. 6. C-rate analysis of the LiNa6-2, LiNa6-4, LiNa6-6, and G-LFP samples.

Table 4
EIS model fitting parameters of all cells.

Cell	Rs	R	Wx10^{-3}	Qy x 10^{-5}	Qa	C x10^{-3}
LiNa6-2	6.11 ± 0.8	658 ± 20	1.75 ± 0.2	4.65 ± 0.2	0.622 ± 0.02	67 ± 0.2
LiNa6-4	7.88 ± 0.7	746 ± 16	2.56 ± 0.2	1.51 ± 0.1	0.777 ± 0.01	31 ± 0.3
LiNa6-6	2.57 ± 0.2	548 ± 15	1.42 ± 0.1	1.45 ± 0.1	0.774 ± 0.02	6 ± 0.1
G-LFP	3.46 ± 0.3	724 ± 9	6.6 ± 0.01	1.14 ± 0.1	0.786 ± 0.02	6 ± 0.1

both techniques and the initial capacities of LiNa6-6 which is the best cell among them for C/10 and 1C were found as 111.1 and 52.5 mAh/g, respectively. In this study, we suggested that the chronoamperometry technique for the production of ion exchange cathodes has a similar effect to the galvanostatic technique and has the advantage of a shorter experiment time, as the chronoamperometry technique requires 12 h and the galvanostatic technique requires 40 h. The diffusion coefficient (D) was found that it was increased by increasing environmental temperature. The full-cell studies exhibited that the capacities of the cells were around 74 mAh/g for the 2–4 The full-cell investigations revealed that the cells' capacity values for the 2–4 V range were approximately 74 mAh/g, which is encouraging for future battery research.

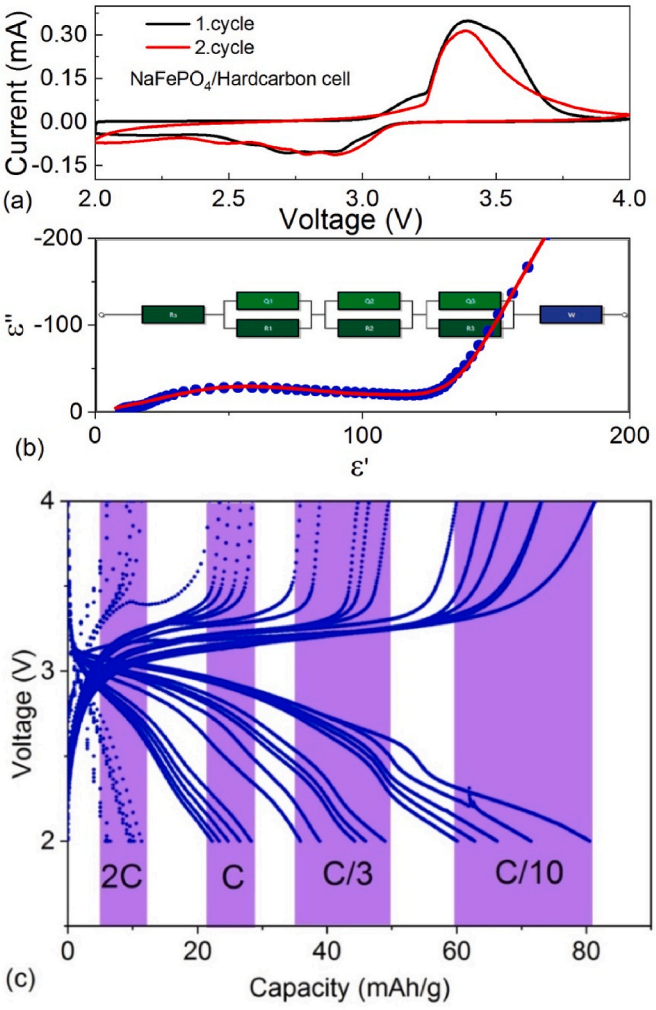

Fig. 7. (a) CV, (b) EIS and (c) C-rate of the NaFePO4/hard-carbon full cell.

CRediT authorship contribution statement

S. Altundag: Methodology, Investigation, Funding acquisition, Formal analysis. **S. Altin:** Writing – original draft, Methodology, Investigation, Funding acquisition. **S. Yaşar:** Writing – review & editing, Writing – original draft, Investigation. **E. Altin:** Writing – review & editing, Writing – original draft, Methodology, Investigation, Formal analysis.

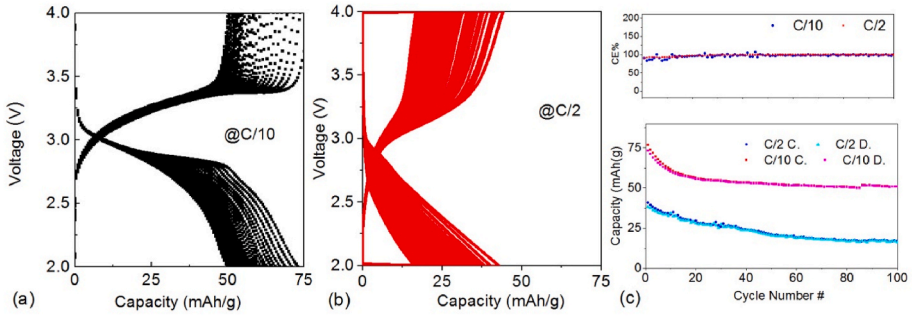

Fig. 8. Capacity-voltage graphs for (a) C/10, (b) C/2, and (c) Capacity-cycle number graphs of $NaFePO_4$/hard carbon full cells.

Declaration of competing interest

The authors declare that they have no known competing financial interests or personal relationships that could have appeared to influence the work reported in this paper.

Data availability

Data will be made available on request.

Acknowledgment

Prof. Dr. Serdar ALTIN also would like to thank the İnönü University Research Council for the Battery performance tests of the devices performed by the budget of FBA-2021-2417.

Appendix A. Supplementary data

Supplementary data to this article can be found online at https://doi.org/10.1016/j.vacuum.2023.111853.

References

[1] Y. Huang, The discovery of cathode materials for lithium-ion batteries from the view of interdisciplinarity, Interdisciplinary Mater. 2 (2021) 323–329.
[2] J.-M. Tarascon, Na-Ion versus Li-ion batteries: complementarity rather than competitiveness, Joule 2 (2020) 1616–1620.
[3] C.-J. Yu, Y.-C. Pak, C.-H. Kim, J.-S. Kim, K.-C. Ri, K.-H. Ri, S.-H. Choe, S. Cottenier, Structural and electrochemical trends in mixed manganese oxides $Na(M_{0.44}Mn_{0.56})O$ (M = Mn, Fe, Co, Ni) for sodium-ion battery cathode, J. Power Sources 511 (2021), 230395.
[4] Y. Fang, Q. Liu, L. Xiao, X. Ai, H. Yang, Y. Cao, A high-performance olivine $NaFePO_4$ microsphere cathode synthesized by aqueous electrochemical displacement method for Na ion batteries, ACS Appl. Mater. Interfaces 7 (2015) 17977–17984.
[5] K. Shiprath, H. Manjunatha, A. Ratnamala, S. Ramesh, K.C. Babu Naidu, Electrochemical study of $NaFePO_4$ cathode material in aqueous sodium-ion electrolyte, Biointerface Research in Applied Chemistry 13 (2021) 186.
[6] M. Nakayama, S. Yamada, R. Jalem, T. Kasuga, Density functional studies of olivine-type $LiFePO_4$ and $NaFePO_4$ as positive electrode materials for rechargeable lithium and sodium ion batteries, Solid State Ionics 286 (2016) 40–44.
[7] C. Heubner, S. Heiden, M. Schneider, A. Michaelis, In-situ preparation and electrochemical characterization of submicron sized $NaFePO_4$ cathode material for sodium-ion batteries, Electrochim. Acta 233 (2017) 78–84.
[8] F. Rahmawati, D.A.N. Romadhona, D.D. Paramita, W.W. Lestari, Preparation of a $NaFePO_4$ cathode material via electrochemical sodiation of $FePO_4$ layers on Al substrates, Int. J. Technol. 13 (2022) 168–178.
[9] N. Wongittharom, T.-C. Lee, C.-H. Wang, Y.-C. Wang, J.-K. Chang, Electrochemical performance of Na/$NaFePO_4$ sodium-ion batteries with ionic liquid electrolytes, J. Mater. Chem. 2 (2014) 5655.
[10] M. Casas-Cabanas, V.V. Roddatis, D. Saurel, P. Kubiak, J. Carretero-Gonzalez, V. Palomares, P. Serras, T. Rojo, Crystal chemistry of Na insertion/deinsertion in $FePO_4$–$NaFePO_4$, J. Mater. Chem. 22 (2012), 17421.
[11] W. Tang, X. Song, Y. Du, C. Peng, M. Lin, S. Xi, B. Tian, J. Zheng, Y. Wu, F. Pan, K. Ping Loh, High-performance $NaFePO_4$ formed by aqueous ion-exchange and its mechanism for advanced sodium ion batteries, J. Mater. Chem. 4 (2016) 4882.
[12] S.-M. Oh, S.-T. Myung, J. Hassoun, B. Scrosati, Y.-K. Sun, Reversible $NaFePO_4$ electrode for sodium secondary batteries, Electrochem. Commun. 22 (2012) 149–152.
[13] Mei-ying Zheng, Zong-yao Bai, Yue-Wen He, Shunqing Wu, Yong Yang, Zi-Zhong Zhu, Anionic redox processes in maricite- and Triphylite-NaFePO4 of sodium-ion batteries, ACS Omega 5 (2020) 5192–5201.
[14] J. Lu, S. Cheong Chung, S-i. Nishimura, A. Yamada, Phase diagram of olivine Na_xFePO_4 ($0 < x < 1$), Chem. Mater. 25 (2013) 4557–4565.
[15] A. Yolun, E. Altin, S. Altundag, M. Arshad, S. Mustansar Abbas, S. Altin, Investigation of structural and electrochemical performance of Ru-substituted $LiFePO_4$ cathode material: an improvement of the capacity and rate performance, J. Mater. Sci. Mater. Electron. 33 (2022) 6670–6680.
[16] S. Altin, A. Yolun, Fabrication and electrochemical performance of Hosubstituted C/$LiFePO_4$: improved battery performance, J. Mater. Sci. Mater. Electron. 32 (2021) 21568–21578.
[17] T. Teng, L. Xiao, L. Shen, G. Qiu, J. Ran, X. Guo, Y. Zhu, H. Chen, Effect of Nb doping at Fe site on the cycling stability and rate capability of LiFePO4 for lithium-ion batteries, Vacuum 203 (2022), 111306.
[18] G. Greczynski, L. Hultman, The same chemical state of carbon gives rise to two peaks in X-ray photoelectron spectroscopy, Sci. Rep. 11 (2021), 11195.
[19] G. Greczynski, L. Hultman, C 1s peak of adventitious carbon aligns to the vacuum level: dire consequences for material's bonding assignment by photoelectron spectroscopy, ChemPhysChem 18 (2017) 1507.
[20] G. Greczynski, L. Hultman, Compromising science by ignorant instrument calibration—need to revisit half a century of published XPS data, Angew. Chem. 59 (2020) 5002.
[21] G. Greczynski, L. Hultman, Reliable determination of chemical state in x-ray photoelectron spectroscopy based on sample-work-function referencing to adventitious carbon: resolving the myth of apparent constant binding energy of the C 1s peak, Appl. Surf. Sci. 451 (2018) 99–103.
[22] G. Greczynski, L. Hultman, A step-by-step guide to perform x-ray photoelectron spectroscopy, J. Appl. Phys. 132 (2022), 011101.
[23] I. Stenina, P. Minakova, T. Kulova, A. Yaroslavtsev, Electrochemical properties of $LiFePO_4$ cathodes: the effect of carbon additives, Batteries 8 (2022) 111.
[24] M.P. Seah, Post-1989 calibration energies for X-ray photoelectron spectrometers and the 1990 Josephson constan, Surf. Interface Anal. 14 (1989) 433–490.
[25] G. Greczynskia, L. Hultman, A step-by-step guide to perform x-ray photoelectron spectroscopy, J. Appl. Phys. 132 (2022), 011101.
[26] G. Grezcynski, L. Luthman, Reliable determination of chemical state in x-ray photoelectron spectroscopy based on sample-work-function referencing to adventitious carbon: resolving the myth of apparent constant binding energy of the C 1s peak, Appl. Surf. Sci. 451 (2018) 99–103.
[27] M. Li, Q. Wang, J. Xu, J. Zhang, Z. Qi, X. Zhang, Optically induced field-emission source based on aligned vertical carbon nanotube arrays, Nanomaterials 11 (2021) 1810.
[28] A. Eugene, Mechtly, properties of materials, Reference Data for Engineers (Ninth Edition), Radio, Electronics, Computer, and Communications 4 (2002) 4–33.
[29] P. Moreau, D. Guyomard, J. Gaubicher, F. Boucher, Structure and stability of sodium intercalated phases in olivine $FePO_4$, 6, Chem. Mater. 22 (2010) 4126–4128.
[30] A. Ait-Salah, J. Dodd, A. Mauger, R. Yazami, F. Gendron, C.M. Julien, Structural and magnetic properties of LiFePO4 and lithium extraction effects, Z. Anorg. Allg. Chem. 632 (2006), 15981605.
[31] Z.C. Shi, A. Attia, W.L. Ye, Q. Wang, Y.X. Li, Y. Yang, Synthesis, characterization and electrochemical performance of mesoporous FePO4 as cathode material for rechargeable lithium batteries, Electrochim. Acta 53 (2008) 2665–2673.
[32] N. Kishor Mal, A. Bhaumik, M. Matsukata, M. Fujiwara, Syntheses of mesoporous hybrid iron oxophenyl phosphate, iron oxophosphate, and sulfonated oxophenyl phosphate, Ind. Eng. Chem. Res. 45 (2006) 7748–7751.
[33] D. White, K. Seshadri, D. Dever, D. Mann, M. Linevsky, Infrared spectra and the structures and thermodynamics of gaseous Lio, Li2O, and Li2O2, J. Chem. Phys. 39 (1963) 2463–2473.
[34] N.V. Kosova, A.B. Slobodyuk, O.A. Podgornova, Comparative structural analysis of LiMPO4 and Li2MPO4F (M = Mn, Fe, Co, Ni) according to XRD, IR, and NMR spectroscopy data, J. Struct. Chem. 57 (2016) 345–353.
[35] X. Ma, J. Xia, X. Wu, Z. Pan, P.K. Shen, Remarkable enhancement in the electrochemical activity of maricite NaFePO4 on high-surface-area carbon cloth for sodium-ion batteries, Carbon 146 (2019) 78–87.

[36] C. Murugesan, S. Lochab, B. Senthilkumar, P. Barpanda, Earth-abundant alkali iron phosphates (AFePO4) as efficient electrocatalysts for the oxygen reduction reaction in alkaline solution, ChemCatChem 10 (2018) 1122–1127.
[37] D. Wyrzykowski, E. Hebanowska, G. Nowak-Wiczk, M. Makowski, L. Chmurzynski, ´Thermal behaviour of citric acid and isomeric aconitic acids, J. Therm. Anal. Calorim. 104 (2011) 731–735.
[38] S.N. Yadav, S.J. Rajoba, R.S. Kalubarme, V.G. Parale, L.D. Jadhav, Solution combustion synthesis of NaFePO4 and its electrochemical performance, Chin. J. Phys. 69 (2021) 134–142.
[39] Zhiwei Wu, Yaguang Li, Linjie Gao, Shufang Wang, Guangsheng Fu, Synthesis of Na doped ZnO Hollow spheres with improving photocatalytic activity for hydrogen production, Dalton Trans. 45 (2016) 11145–11149.
[40] M. Faisal, Sher Bahadar Khan, Mohammed M. Rahman, Aslam Jamal, M. M. Abdullah, Fabrication of ZnO nanoparticles based sensitive methanol sensor and efficient photocatalyst, Appl. Surf. Sci. 258 (2012) 7515–7522.
[41] https://www.thermofisher.com/tr/en/home/materials-science/learning-center/periodic-table/non-metal/carbon.html.
[42] S.H. Song, J.M. Kim, K.H. Park, D.J. Lee, O.-S. Kwon, J. Kim, H. Yoon, X. Chen, High performance graphene embedded rubber composites, RSC Adv. 5 (2015) 81707–81712.
[43] M.L. Kalapsazova, E.N. Zhecheva, G.T. Tyuliev, D.D. Nihtianova, L. Mihaylov, R. K. Stoyanova, Effects of the particle size distribution and of the electrolyte salt on the intercalation properties of P3-Na2/3Ni1/2Mn1/2O2, J. Phys. Chem. C 121 (2017) 5931–5940.
[44] M. Kalapsazova, R. Stoyanova, E. Zhecheva, G. Tyuliev, D. Nihtianova, Sodium deficient nickel–manganese oxides as intercalation electrodes in lithium ion batteries, J. Mater. Chem. 2 (2014), 19383.
[45] A. Rjan, M. Sharma, N.K. Sahu, Assessing magnetic and inductive thermal properties of various surfactants functionalised Fe3O4 nanoparticles for hyperthermia, Sci. Rep. 10 (2020), 15045.
[46] G.A. Alnawashi, A.M. Alsmadi, I. Bsoul, B. Salameh, G.M. Alzoubi, M. Shatnawi, S. M. Hamasha, S.H. Mahmood, Investigation on X-ray photoelectron spectroscopy, structural and low temperature magnetic properties of Ni-Ti co-substituted M-type strontium hexaferrites prepared by ball milling technique, Results Phys. 28 (2021), 104574.
[47] T. Yamashita, P. Hayes, Analysis of XPS spectra of Fe2+ and Fe3+ ions in oxide materials, Appl. Surf. Sci. 254 (2008) 2441.
[48] K. Idczak, R. Idczak, Investigation of surface segregation in Fe-Cr-Si alloys by XPS, Metall. Mater. Trans. 51 (2020) 3076.
[49] R. Tatara, P. Karayaylali, Y. Yu, Y. Zhang, L. Giordano, F. Maglia, R. Jung, J. P. Schmidt, I. Lund, Y.S. Horn, The effect of electrode-electrolyte interface on the electrochemical impedance spectra for positive electrode in Li-ion battery, J. Electrochem. Soc. 166 (2019) 3.
[50] G. Zheng, C. Wu, J. Wang, S. Mo, Z. Zou, B. Zhou, F. Long, Space-confined effect one-pot synthesis of γ-AlO(OH)/MgAl-LDH Heterostructures with excellent adsorption performance, Nanoscale Res. Lett. 14 (2019) 281.
[51] J. Feng, N.A. Chernova, F. Omenya, L. Tong, A.C. Rastogi, M.S. Whittingham, Effect of electrode charge balance on the energy storage performance of hybrid supercapacitor cells based on LiFePO4 as Li-ion battery electrode and activated carbon, J. Solid State Electrochem. 22 (2018) 1063–1078.
[52] J. Triwibowo, S. Priyono, I. Purawiardi, T. Lestariningsih, C.R. Ratri, Study on electrochemical performance of carbon-coated LiFePO4 as cathode material for lithium ion batteries, AIP Conf. Proc. 1755 (2016), 150009.
[53] T. Boyadzhieva, V. Koleva, P. Markov, R. Stoyanova, Iron oxidation to amplify the Na and Li storage capacities of nano-sized maricite NaFePO4, Dalton Trans. 50 (2021) 16548–16561.
[54] Y.-H. Huang, F.-M. Wang, T.-T. Huang, J.-M. Chen, B.-J. Hwang, J. Rick, Micro-electrode linked cyclic voltammetry study reveals ultra-fast discharge and high ionic transfer behavior of LiFePO4, Int. J. Electrochem. Sci. 7 (2012) 1205–1213.
[55] W. Tang, X. Song, Y. Du, C. Peng, M. Lin, S. Xi, B. Tian, J. Zheng, Y. Wu, F. Pan, K. P. Loh, High-performance NaFePO4 formed by aqueous ion-exchange and its mechanism for advanced sodium ion batteries, J. Mater. Chem. 4 (2016) 4882.
[56] S.-M. Oh, S.-T. M, J. Hassoun, B. Scrosati, Y.-K. Sun, Reversible NaFePO4 electrode for sodium secondary batteries, Electrochem. Commun. 22 (2012) 149–152.
[57] Y. Fang, Q. Liu, L. Xiao, X. Ai, H. Yang, Y. Cao, High-performance olivine NaFePO4 microsphere cathode synthesized by aqueous electrochemical displacement method for sodium ion batteries, ACS Appl. Mater. Interfaces 7 (2015), 17977−17984.
[58] A.R.C. Bredar, A.L. Chown, A.R. Burton, B.H. Farnum, Electrochemical impedance spectroscopy of metal oxide electrodes for energy applications, ACS Appl. Energy Mater. 3 (2020) 66–98.
[59] Y. Abe, N. Hori, S. Kumagai, Electrochemical impedance spectroscopy on the performance degradation of LiFePO4/Graphite lithium-ion battery due to charge-discharge cycling under different C-rates, Energies 12 (2019) 4507.
[60] http://zivelab.com/asw/zman23man.pdf.